Supplementary Information

Reversing silicon carbide into 1D-silicon nanowires and graphene-like structures by dynamical magnetic flux template

Wenting Zhou, Qiang Liu, Qingsong Huang*

School of Chemical Engineering, Sichuan University, Chengdu 610065, P. R. China

***Corresponding Email: qshuang@scu.edu.cn**

1. The comparison of amorphous silicon nanowires and crystal silicon nanowires

Table S1 The characteristics of the application of amorphous silicon nanowires and crystal silicon nanowires in some fields.

	a-silicon	c-silicon
Lithium ion cell[1-4]	Reaction potential of a-Si with lithium is 0.22V; High structural fracture resistance; Good cycling performance.	Reaction potential of c-Si with lithium is 0.12V; Poor performance in the charge-discharge characteristics.
Solar cell[5-8]	Higher absorption coefficient; More economical; Poor cell stability.	High power efficiencies; Not good at high temperatures.
Photocatalytic hydrogen production[9-11]	Wide band gap; Absorption of sunlight in a wide range; Larger photovoltage output.	Narrower band gap; Long service life;
Field-effect transistors[12-16]	Can produce drive currents and on/off current ratios adequate for some applications; Low electron mobility;	High sensitivity; Can reduce short-channel effects.

2. The reversing mechanism of SiC

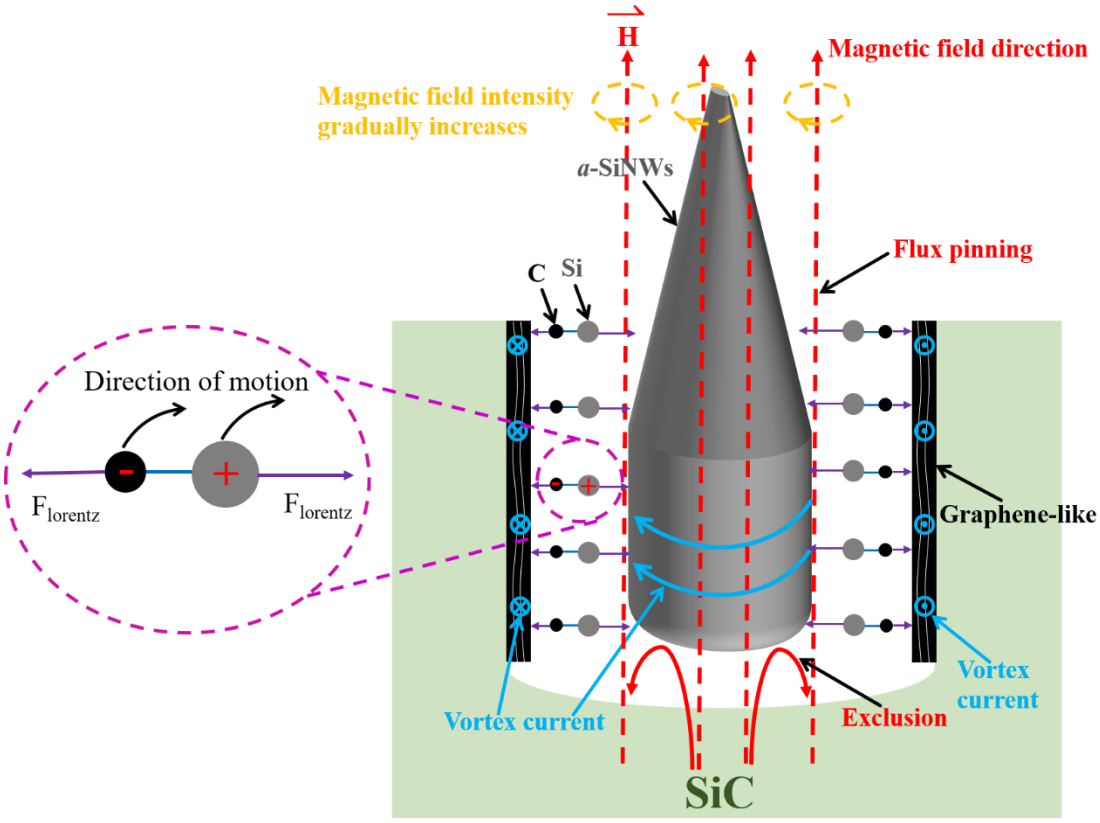

Fig. S1 Schematic diagram of reversing SiC into *a*-SiNW and multilayer graphene composite structure under magnetic field strength increases.

When the dynamic magnetic field is applied, the magnetic flux will penetrate the SiC particles, and the magnetic flux quantum-well forms because of the non-uniform magnetic field and SiC magnetic medium. In the process of reversing SiC, vortex current joule heat, graphite block joule heat, and Lorentz force worked together to break Si-C bond, resulting in polarized silicon and carbon atoms separation. The polarized silicon atoms are collected to the flux well center to form semi-solid silicon paste by both Lorentz force and vortex current, then the silicon is drawn out by repelling force to form amorphous silicon nanowire along the direction of magnetic flux template. While the carbon atoms were forced by Lorentz force to the hole wall to reconstruct into graphene-like because of heating from graphite block and vortex current. In addition, the obtained graphene cannot develop into graphite, because the vortex current prevents graphene sheet from accumulating into graphite AB Bernal stacking configuration.

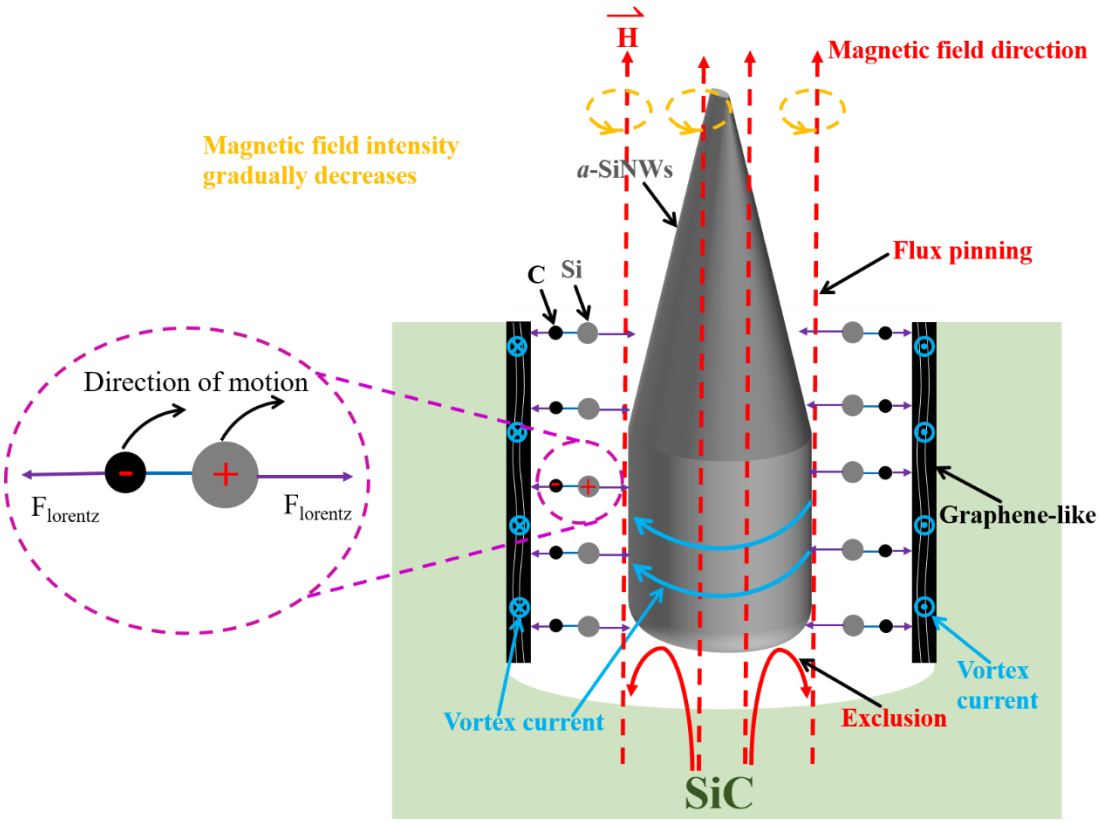

Fig. S2 Schematic diagram of reversing SiC into *a*-SiNW and multilayer graphene composite structure under magnetic field strength decreases.

Since the current input to the induction coil is rectified, the direction of the magnetic field is unchanged. However, the intensity of the magnetic field is change. The clockwise arrows in yellow circle indicate that the magnetic field strength increases (Fig. S1), while the anticlockwise arrows indicate that the strength decreases (Fig. S2).

3. The magnetic field strength

A fluxmeter was used to characterize the magnetic field strength. The probe of fluxmeter on the setting measurement points were marked with blue、red and green colors (Fig. S3), and the measurement is carried out by setting circuit current of 30 A, under atmosphere pressure, and after lasting for 2 s. The magnetic field intensity inside the coil can reach 248.252 mT, which is greater than outside the coil. The intensity becomes decreasing if uploading sample within the coil (Fig. S3, inset data).

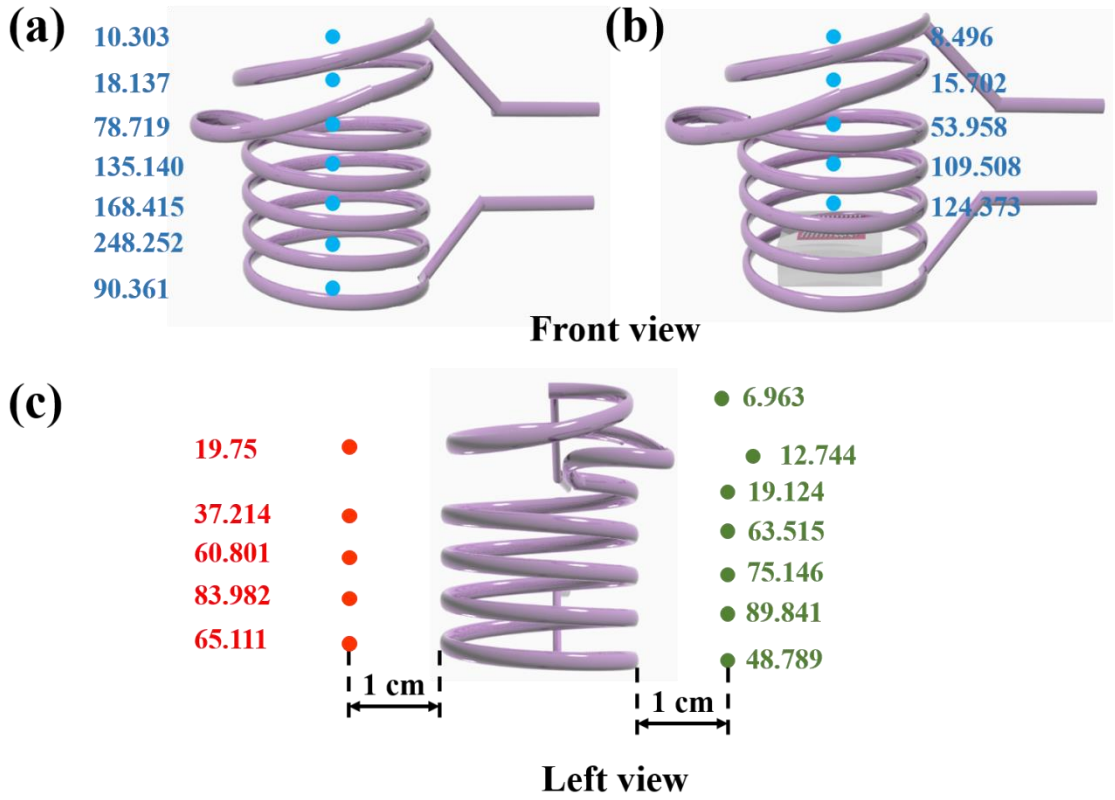

Fig. S3 The magnetic field strength at different positions of the induction coil under 30 A. (Blue, red and green dots represent the measurement locations in the center of coil and outside the coil, respectively; The number of corresponding color indicates field strength, mT). The front view of induction coils without sample (a) and with sample (b). (c) The left view of induction coils without sample.

4. The reaction temperature

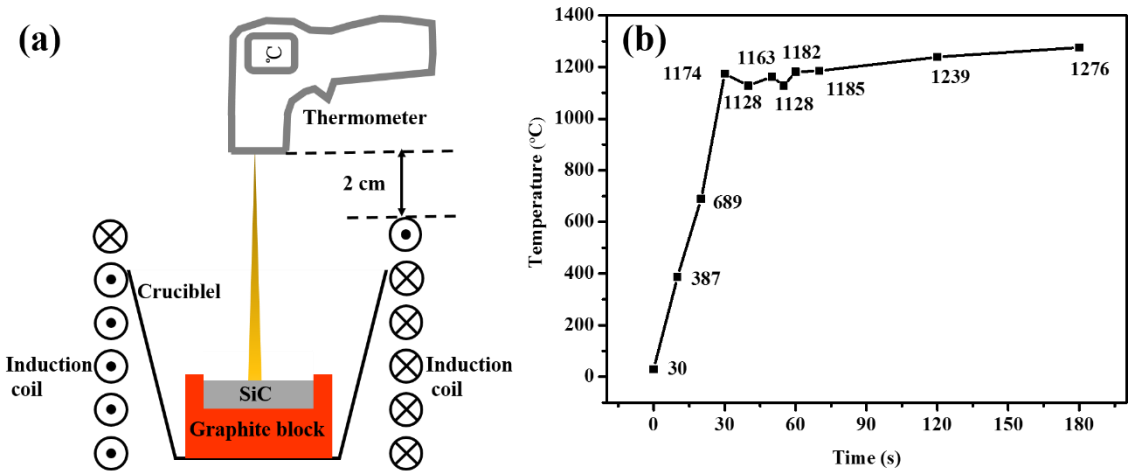

Fig. S4 (a) Schematic diagram of sample temperature measured by infrared thermometer; (b) Curve of sample surface temperature change with time at alternating current of 30 A.

5. The magnetic separation ability

Usually, the magnetic field can be measured and calculated, and its distribution can be described. The charge cannot be influenced by the static magnetic field unless the charge is moving along intersecting rail with magnetic force line according to Faraday's law of electromagnetic induction. However, the dynamic magnetic field (DMF) can influence the charge without motion, since a related induction electronic field can be created from the DMF. Thus, the static magnetic force is influenced by key factors, such as moving velocity, orientation, charge number and so on, suggesting the magnetic force should not be a constant. Actually, even in a same point, the magnetic force cannot be measured or calculated, since the key factors are not constant. Usually, the magnetic force can be from zero to that critical force to break the bond.

As for breaking the bond, it is usually marked with energy unit, because no constant force can be used to evaluate the breaking force, instead, the bonding energy have been adopted to mark the force before.

Here, since the magnetic Lorenz force is distributed within a scope, we try our best to make a rough estimation of the average value. The dynamic magnetic field exerts force on both immobile and mobile Si-C polarized bond. During the process of DMT, the immobile Si-C polarized bond under induced electromotive force can be broken by

both heat energy and magnetic energy. Meanwhile, for the movable Si-C polarized bond, additional magnetic force on polarized bond can be produced by intersection motion with magnetic line. In addition, the energy fluctuation (kT) should also be considered to contribute to the bond breaking. It is difficult to calculate the maximum value of the magnetic force, but the average magnetic force can be roughly calculated through the vibration distance. We would consider the two cases in calculating magnetic force. Reversing SiC at excitation current of 30 A, the temperature of SiC can be heated to around 1174℃ after 30 S. Taking the DMT for 30 s as an example to calculate magnetic energy and average magnetic force:

(1). Magnetic energy-without considering the energy fluctuation

The decomposition equation of SiC is: SiC (sol) = Si (gas) + C (sol), so there is a equation: $\Delta G_T^o(SiC) = RT \ln(P_o/P)$[17, 18].

According to the energy exerted on SiC, there is an equilibrium equation on SiC: $Q = E_{Si\text{-}C\ bond} - RT \ln(P_o/P)$,

Q- magnetic energy;

$E_{Si\text{-}C\ bond}$—bond energy of Si-C;

$RT \ln(P_o/P)$—heat energy: T-temperature; P_o- the partial pressure of silicon over SiC (i.e., the dissociation pressure of SiC; in our experiment P_o is around 10 kPa); $\lg(P) = -18558/T + 11.73$ (in the temperature range 1485–1593 K)[18].

① The bond energy of Si-C is 290 kJ/mol[19], therefore $E_{Si\text{-}C\ bond}$ =290/NA kJ = 3.0 eV (NA-Avogadro constant);

② Heat energy: $RT \ln(P_o/P)$ = 1.5 eV;

③ The energy required to destroy a Si-C bond: $Q_1 = E_{Si\text{-}C\ bond} - RT \ln(P_o/P)$ =1.5 eV;

④ The energy required to destroy four Si-C bonds: Q_4 =1.5 eV*4 = 6.0 eV.

(2). Magnetic energy- with considering the energy fluctuation

$Q = E_{Si\text{-}C\ bond} - RT \ln(P_o/P) - kT$

kT-vibration energy: k- boltzmann constant.

① Vibration energy: kT = 0.1 eV

② The energy required to destroy a Si-C bond: $Q_1 = E_{Si\text{-}C\ bond} - RT\ \ln(P_o/P) - kT$ = 1.4 eV;

③ The energy required to destroy four Si-C bonds: Q_4 = 1.4 eV*4 = 5.6 eV.

The calculation results were listed in Table S2, which illustrates the required magnetic field energy for breaking a Si-C bond is between 1.4 eV and 1.7 eV.

Table S2 Magnetic energy required for breaking Si-C bond under different temperature.

	1 Si-C bond/ eV	2 Si-C bonds/ eV	3 Si-C bonds/ eV	4 Si-C bonds/ eV
1174℃ (30 s)	1.4-1.5	2.8-3.0	4.2-4.5	5.6-6.0
1182℃ (60 s)	1.4-1.5	2.8-3.0	4.2-4.5	5.6-6.0
1276℃ (180 s)	1.6-1.7	3.2-3.4	4.8-5.1	6.4-6.8

(3). Average magnetic force

The magnetic force is inconstant. Here we use the average force to approximately describe the effect of the magnetic field. The relation between magnetic force and magnetic energy is: Q = F*S, where the S is displacement, the F is average magnetic force. The van der Waals radii of silicon is R_{Si} =0.21 nm, van der Waals radii of carbon is R_C =0.17 nm[20], the bond length of Si-C bond is $L_{Si\text{-}C}$ =0.19 nm[21]. So the displacement $S = R_{Si} + R_C - L_{Si\text{-}C}$. According Table S2 and the equation F = Q/S to calculate average magnetic force, which was listed in Table S3.

Table S3 Magnetic force required for Si-C bond breaking under different temperature.

	1 Si-C bond/ 10^{-9} N	2 Si-C bonds/ 10^{-9} N	3 Si-C bonds/ 10^{-9} N	4 Si-C bonds/ 10^{-9} N
1174℃ (30 s)	1.2-1.3	2.4-2.5	3.5-3.8	4.7-5.1
1182℃ (60 s)	1.2-1.3	2.4-2.5	3.5-3.8	4.7-5.1
1276℃ (180 s)	1.3-1.4	2.7-2.9	4.0-4.3	5.4-5.7

6. The holes structure on SiC after removing silicon nanowires

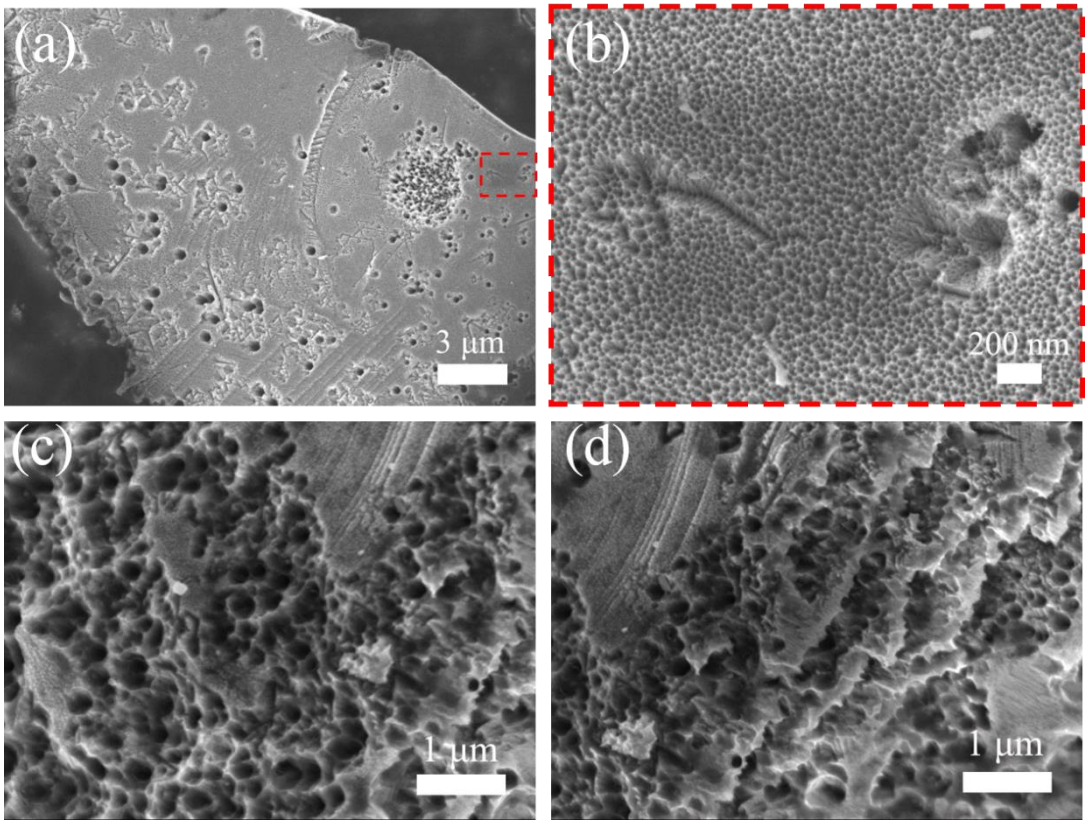

Fig. S5 The surface porous structure on SiC (6H-SiC, under 30 A, 10 kPa and 180 s) treated under DMT route and washed successively with hydrofluoric acid sonification. (a) Two kinds of hole can be observed, and the larger holes are partly inheriting from the micro-tubes as raw materials, and the smaller ones is created by the magnetic flux well. (b) The magnified image of the red frame in (a), where the hole's size is as small as those of silicon nanowire. (c-d) Some larger hole can be created by flux well, which can accommodate the silicon wires in coarse diameter.

7. Magnetic flux template (DMT) confines the growing orientation of silicon nanowires and bearing the wire weight

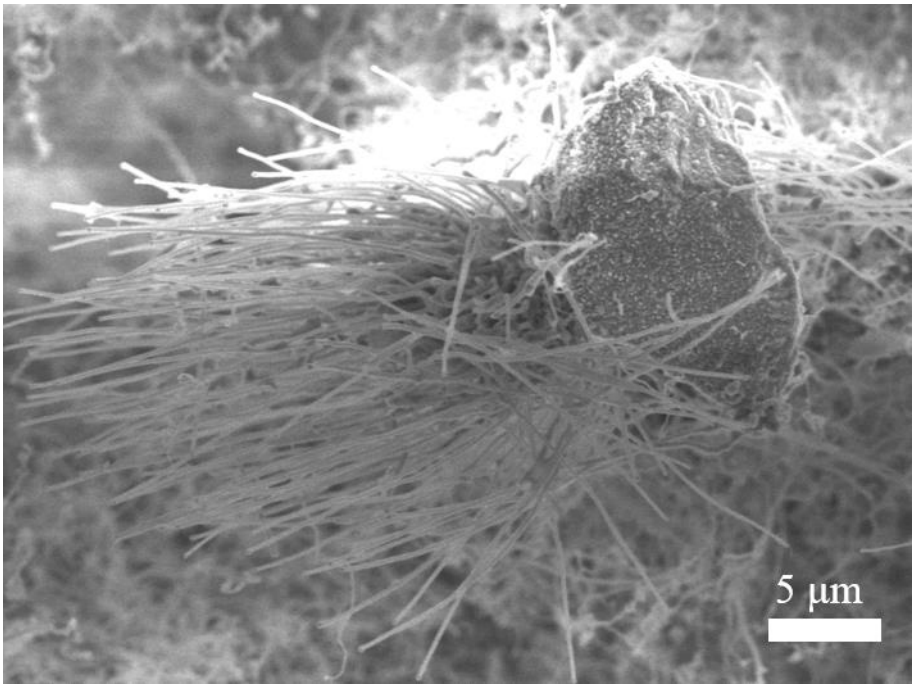

Fig. S6 SiNWS@SiC composite structures, where the wires were pinned by DMT. The typical characteristics of paralleling nanowires suggest that the wires grow along the flux orientation and are supported by the DMT magnetic lines.

8. The left carbon structure after SiC has been almost decomposed completely

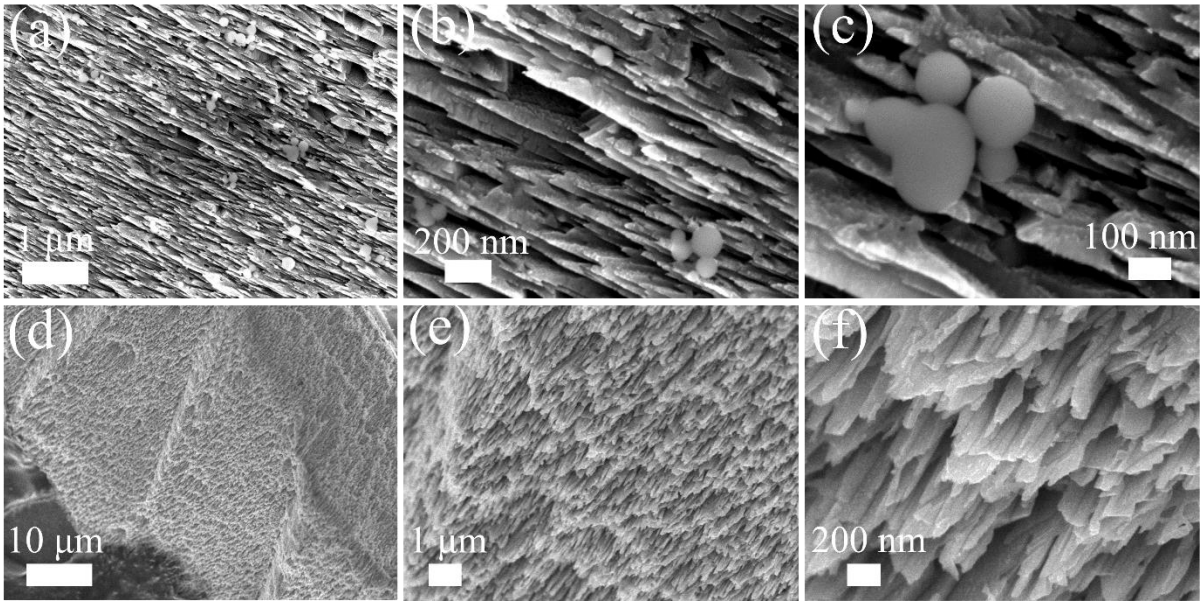

Fig. S7 The carbon structure after the silicon has been exhausted by DMT technique. (a-c) When the silicon evaporates in high temperature, some silicon spheres formed because of the condensation of silicon vapor. (d-f) From (d) to (f), the carbon structures have been enlarged gradually. In the (f), the carbon has been reconstructed into graphene against the hole wall.

Two situations have been observed. (1) If the growth temperature is too high to sustain the silicon in the paste state, it should be evaporated into vapor, and high-pressure silicon vapor will become nucleation and condensed into silicon spheres during the cooling process (Fig. S7 (a-c)). (2) if the growth temperature can sustain the silicon paste state, the silicon in silicon carbide can be removed completely (Fig. S7 (d-f)). Moreover, the silicon vapor pressure is very low, so that the silicon vapor cannot form nuclei on the surface particles.

In addition, during the process of extracting silicon out of the silicon carbide, the left carbon atoms were driven to the wall of holes, and reconstructed into graphene (Fig. S7 (f)). Despite the graphene layer can form one layer by one layer, they refused to evolution into graphite (Fig. S7 (f)), because of the interference of vortex current.

9. Amorphous silicon nanowires on a large scale

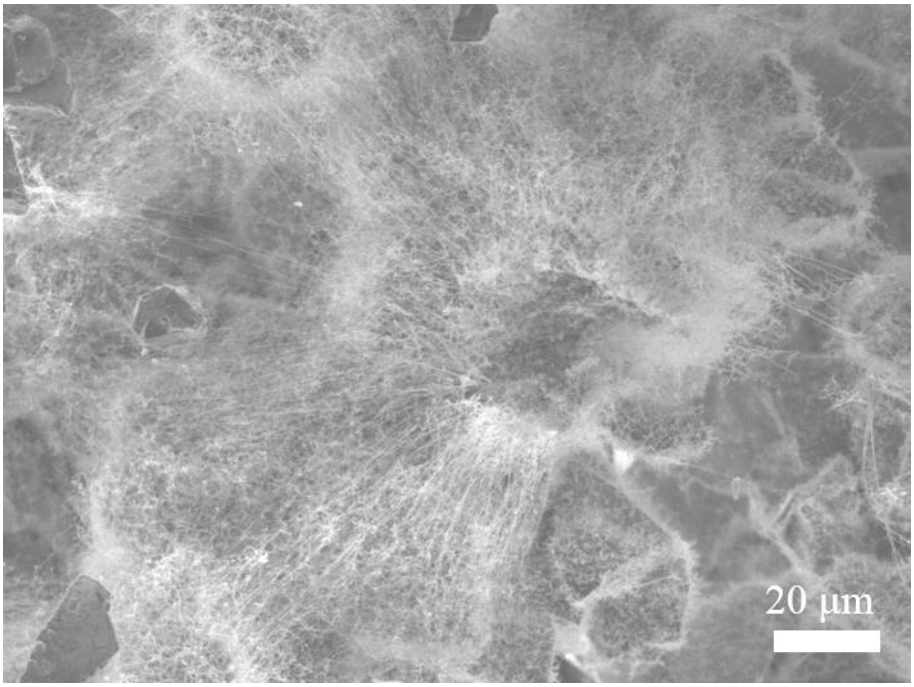

Fig. S8 Silicon nanowires on a large scale. A large number of amorphous silicon nanowires obtained by reversing silicon carbide.

There are a large-area silicon nanowires cover on the silicon carbide particle surface. The DMT method provides a new way for synthesizing large-scale amorphous silicon nanowires.

10. Growth rate of silicon nanowires

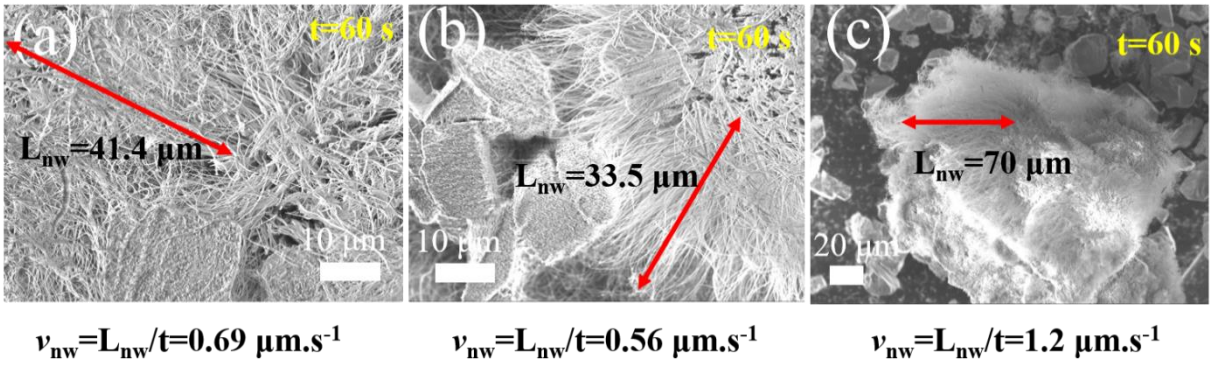

Fig. S9 The growth rate of silicon nanowires under same condition. An average growth rate can be calculated according to the different SiC particles, (a) V_{nw}= 0.69 μm.s^{-1}, (b) V_{nw}= 0.56 μm.s^{-1} and (c) V_{nw}= 1.2 μm.s^{-1}. The average rate should be around 0.82 μm.s^{-1}.

Upon the reaction time reaching 60 s, the growth of amorphous silicon nanowires can be observed in Fig. S9 (a-c). Under same process, the three different silicon carbide particles were collected to measure the growth rate, and an average rate has been calculated.

11. Comparison of preparation methods of silicon nanowires

Table S4 The synthesis methods of silicon nanowires.

Method	Method characteristics	Results	Advantages /disadvantages	Ref.
Dynamic magnetic flux template (DMT)	Silicon carbide as raw material decomposes into silicon, which forms silicon nanowires under the constraint of magnetic flux template	Pure silicon nanowires with a diameter of 10-200 nm and a length of 70 microns in 60s	Short growth time, simple process, low cost/ require dynamic magnetic field	This paper
Chemical vapor deposition (CVD)	Need a volatile gaseous silicon source, such as SiH_4 or $SiCl_4$. The catalyzers are to form a alloy with Si, which acts as a sink for species from the vapor phase	The diameter of NWs ranges from 10nm to several hundred micrometers	The length and diameter of NWs with a large rang/use potentially dangerous precursor gases	22-25
Molecular beam epitaxy (MBE)	Constituent pure silicon are thermally evaporated in an ultra-high vacuum. The evaporants are deposited epitaxially onto substrates.	The diameters of NWs exceeds 40 nm	Low reaction temperature/require ultra-high vacuum, low nanowires growth velocity	26-28
Laser ablation (LA)	Pulsed laser ablates material from a mixed Si–catalyst target	The average diameter of nanowires is small (up to 8 nm)	Large quantities of nanowires/require expensive high-power pulsed laser	29-31
Solution–liquid–solid	Highly pressurized supercritical organic	Large volume and small diameter of	Suitable for mass production/high reaction	32, 33

	fluids enriched with a liquid Si precursor and metal catalyst particles were utilized to synthesize SiNWs	defect-free SiNWs	pressure	
Oxide-assisted method (OAG)	Thermal evaporation and disproportionation of SiO	Silicon oxide layer on the outside of nanowires	Simple operation/not yielded a good control over diameter	1, 23, 34, 35
Solid-liquid-solid	Silicon source comes from silicon substrate	Silicon nanowires do not contain metal catalysts	A relatively simple and straightforward method to grow large amount of NWs/the dimension and direction of nanowires could not be controlled	26, 36-38
Metal-assisted chemical etching (MACE)	Metal-induced chemical etching of silicon substrates in HF solution.	Large area and highly oriented silicon nanowire arrays	Simplicity, large scale production/metal-induced contamination, hard to control the wire diameter and interspacing	26, 32, 39
Reactive ion etching (RIE)	The etched object generates volatile gas under the physical bombardment and chemical reaction of reactive ions, and the part protected by the mask remains	Vertical nanowire arrays	Precise control over a wide range of diameters and spacings/expensive equipment and complex process	40-42
Electrodeposition	Liquid phase (containing silicon source) solidifies on template (such as polycarbonate) through chemical reaction	The size of nanowires is up to template size	Room temperature deposition, no metal catalyst/require expensive ionic liquid	23, 43
Electron-beam lithography (EBL)	Using a silicon-on-insulator (SOI) fabrication technique	Silicon nanowires with precisely controlled diameter and length	High resolution and great flexibility/require sophisticated instruments, expensive production cost	1, 44

Table S4 list some advantages and disadvantages of various silicon nanowire preparation methods. At present, there are certain problems in the previous preparation methods of silicon nanowires. The vapor-liquid-solid (VLS) method should perhaps introduce catalyst pollution problems[45], moreover, undergoing the solid-liquid-solid process, the dimension and direction of nanowires could not be controlled efficiently[26]. Laser ablation and electrochemical deposition need expensive equipment, such as the high-energy focused pulsed lasers and ionic liquid, respectively[24, 46]. RIE requires complex process, so it is difficult to prepare nanowire in large areas. The MACE method has metal-induced contamination[47]. The OAG method cannot control over diameter of nanowires well[23].

As for our DMT method, the most important is the magnetic flux template itself. The DMT can be quickly established and revoked without introducing any pollution. In addition, The DMT behaves like a template for guiding the orientation, bearing a 1D silicon structure, activating the nucleation, and providing a driving force for silicon nanowire growth. The superfast growth can be realized via DMT route within a few minutes. Moreover, the preparation process is simple and does not cause environmental pollution. The limitation of DMT method is requiring dynamic magnetic field.

12. Effect of the constant magnetic field on growing Si nanowires

According to the mechanism of DMT reversing silicon carbide, the decomposition of silicon carbide requires around 1000~1100 ℃ and magnetic field. As shown on Fig. S10, we mimic the same condition with a CVD tube furnace and graphite to heat the same kind of SiC. A constant magnetic field is fixed on the top of tubular furnace, where the magnetic field is arising from the NdFeB permanent magnet, which can be sustained from changing. The magnetic field near the sample is 70-100 mT. Placing the graphite blocks containing silicon carbide particles in the crucible, then putting them on a constant magnetic field. When temperature reaches ~1050 ºC, the constant magnetic field and temperature can be kept from changing for 3 minutes, mimicking the situation in DMT.

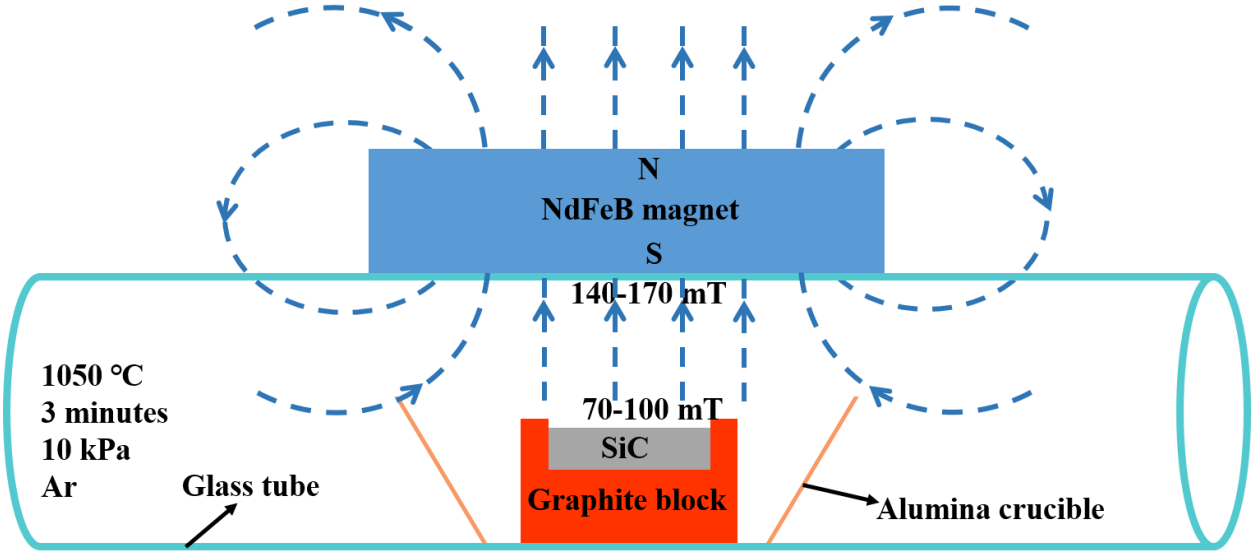

Fig. S10 Schematic diagram of reversing silicon carbide in a constant magnetic field.

The results of reversing silicon carbide in a constant magnetic field are shown in Fig.S11. There are no silicon nanowires on the silicon carbide surface. The DMT can impose a force on the silicon nanowire, but a constant field cannot, because the silicon nanowires are neither charged nor magnetic. Therefore, the growth of silicon nanowires from silicon carbide cannot be realized by heating and imposing constant magnetic field.

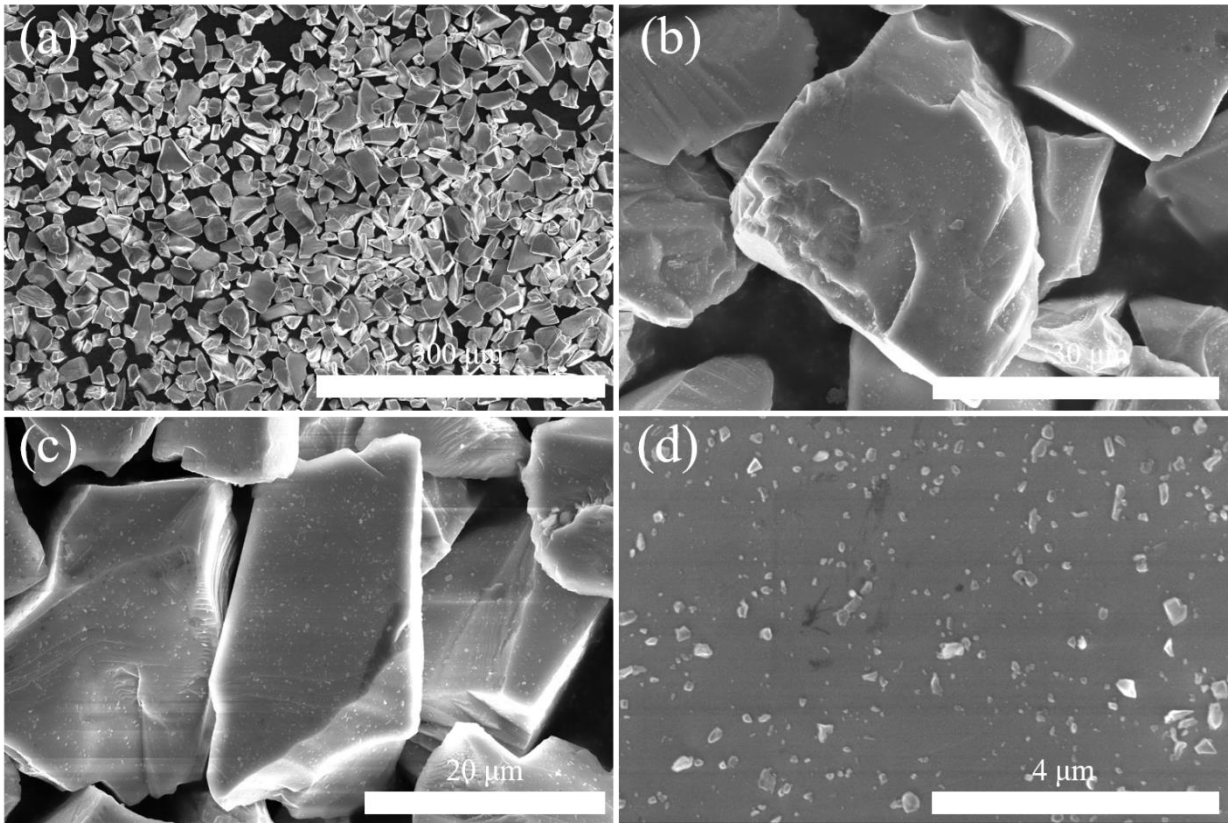

Fig. S11 Surface morphology of silicon carbide. Silicon nanowires cannot be synthesized in a constant magnetic field.

13. Composition analysis of amorphous silicon nanowires

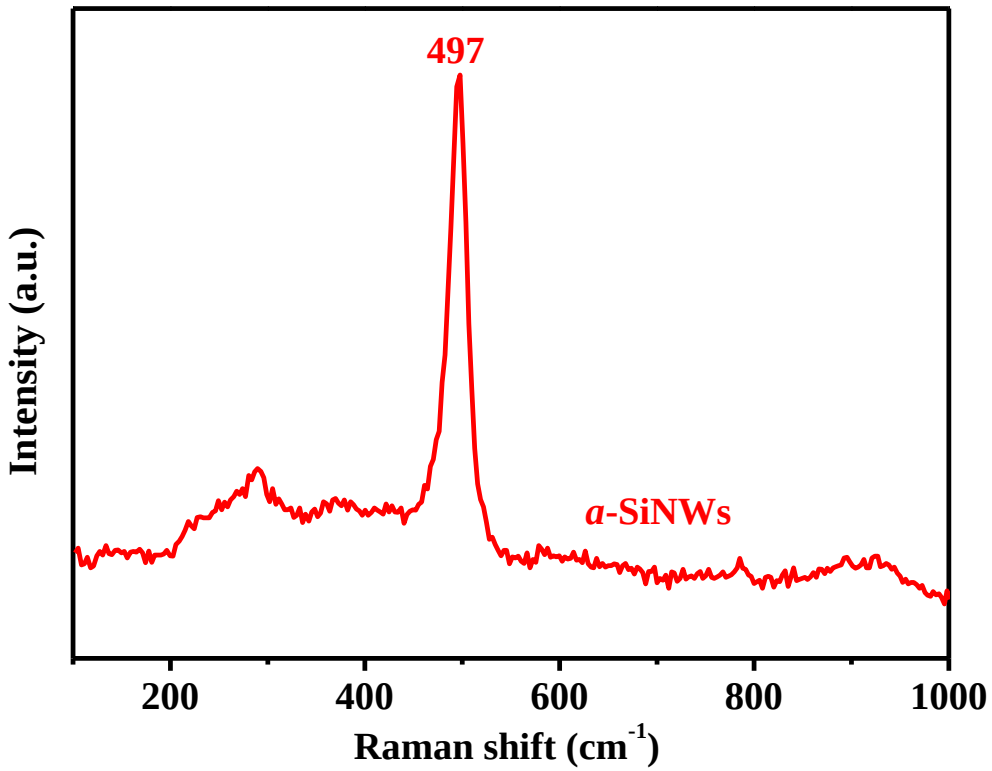

Fig. S12 Raman spectra of *a*-Silicon Nanowires. In the Raman spectrum, the wave number of 497 cm^{-1} is the fingerprint of amorphous silicon.

The Raman spectrum of the silicon nanowires grown by DMT method is show on Fig. S12. The peak of 497cm^{-1} is the characteristic peak of amorphous silicon[48].

14. XPS spectra of SiNWS@SiC

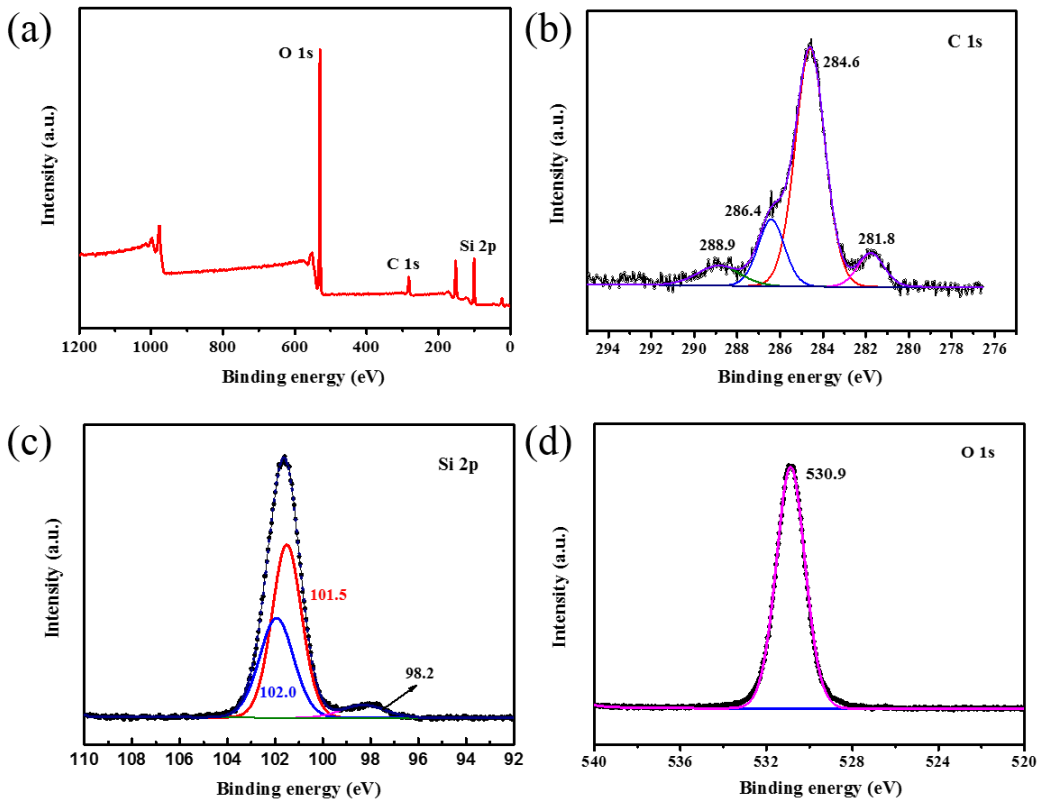

Fig. S13 (a) XPS spectra of reversed silicon carbide. XPS spectra of (b) C 1s, (c) Si 2p, (d) O 1s.

15. Silicon nanowires cannot be prepared through heating silicon carbide only

Table S5 The products obtained by heating SiC materials under different reaction conditions

Material	Pressure	Temperature	Atmosphere	Products
4H-SiC wafers [49]	90 kPa and 0.001 Pa	1600 ° C	95% Ar with 5%H_2	Standing graphene strips
6H–SiC wafers [50]	1×10^{-4} Torr	1700 ℃	Air	Carbon nanotube、graphite
6H–SiC particals [51]	0.2 atmosphere	1100℃	Ar	Graphene films
6H–SiC wafers [52]	1 atm or 1 atm+5 kPa	1550℃	95% Ar with 5 % H_2	Crystalline silicon nanospheres or amorphous silicon nanospheres
SiC powder [53]	1–5 Pa	1400°C–1600°C	90% Ar and 10% H_2	Graphene sheets
6H-SiC powder [54]	1×10^{-3} Pa	1600℃	95% Ar with 5 % H_2	Graphene layers
6H–SiC wafers [55]	10-900 mbar	1500°C–2000°C	Ar	Graphene films

Table S5 listed the cutting-edge works over heating silicon carbide particles and silicon carbide wafers under different conditions. We found that silicon nanowires cannot be obtained from silicon carbide materials by heating only under even both negative and positive pressure. The silicon sublimating from silicon carbide was full of the reaction furnace under low pressure, and the left carbon atoms will be reconstructed into graphene if furnace pressure is less than 1 atm, otherwise, silicon nanospheres might form unless the pressure is larger than 1 atm. Therefore, the magnetic field plays a key role in the growth of silicon carbide in the induction furn.

16. The multilayer graphene stripped from hole wall

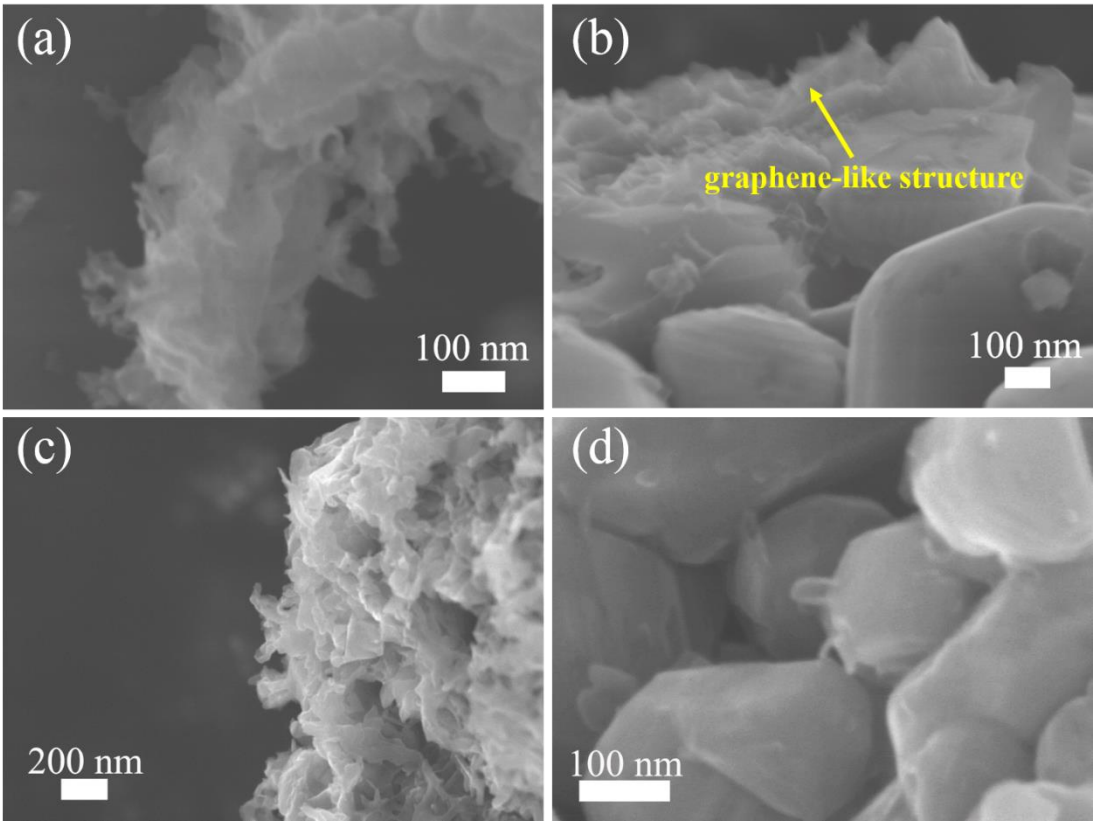

Fig. S14 The morphologies after HF sonification-treated holes, where graphene covers on SiC. (a) The independent multilayer graphene stripped from hole's wall. (b) Graphene formed *in-situ*. (c) An additional hole wall covered by graphene, and (d) when the hole is broken, the graphene can be sustained.

The carbon atoms that produced by silicon carbide decomposition, can be reconstructed into multilayer graphene because of the vortex current and heating from graphite block.

17. Battery performance of original pure silicon carbide and reversed silicon carbide

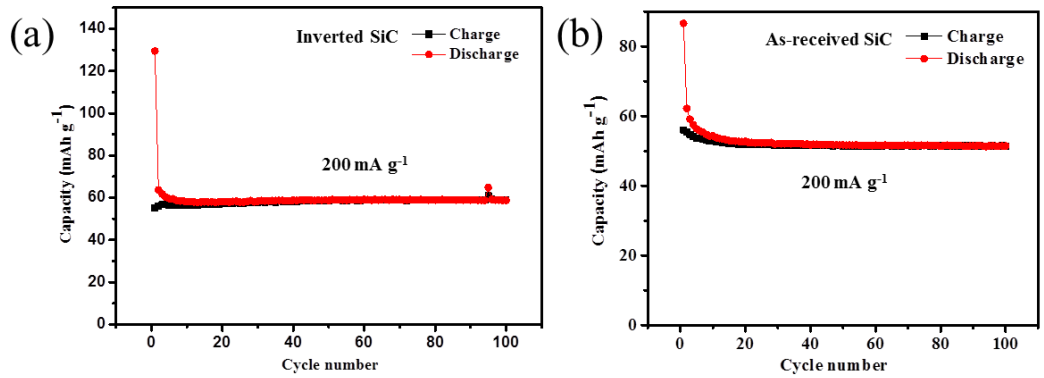

Fig. S15 Cycling behavior of reversed SiC electrode (average capacity - 59 mAh g^{-1}, at a current of 200 mA g^{-1}) (a) and as-received SiC (average capacity - 51 mAh g^{-1}, at a current of 200 mA g^{-1}) (b) cycled using a current of 200 mA g^{-1} for 100 cycles.

18. Silicon nanowires collected by carbon cloth

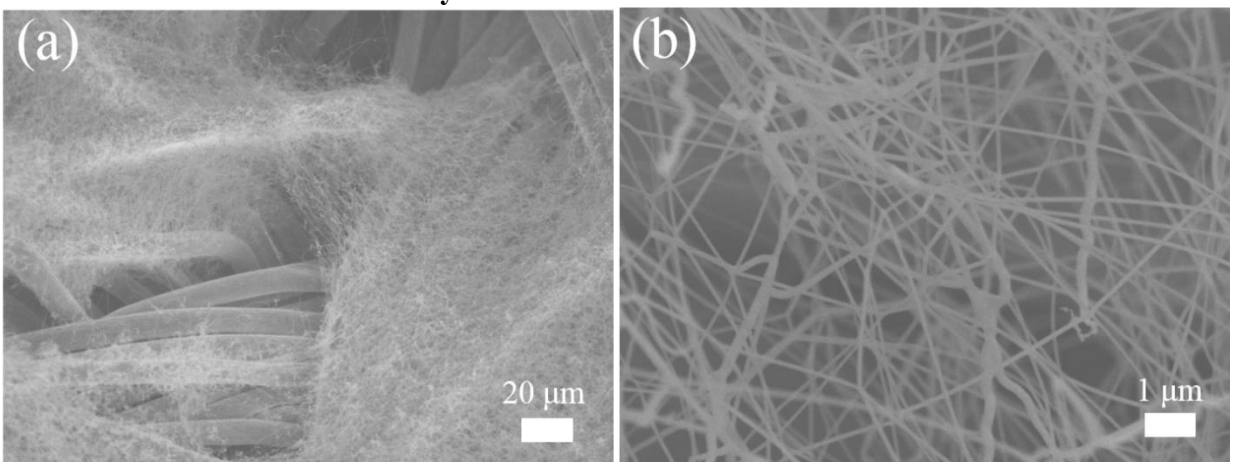

Fig. S16 The morphologies of silicon nanowires collected with carbon cloth at the reaction time of 60 s. (a) The morphology that nanowires covered on carbon cloth. (b) The morphology of silicon nanowires.

19. The half-cell performance of *a*-SiNWs on carbon cloth (*a*-SiNWs/CC) electrode

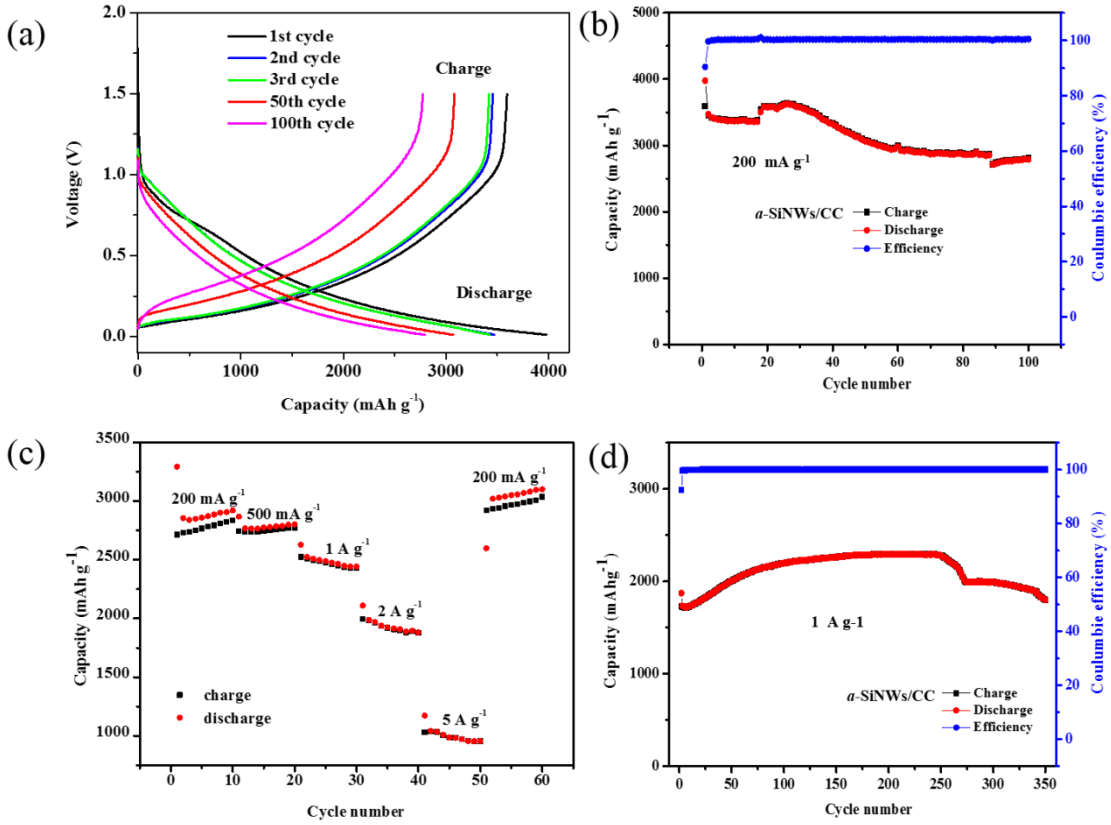

Fig. S17 Electrochemical characterization of a-SiNWs/CC. (a) Galvanostatic cycling curves of an electrode at the 1st, 2nd, 3rd, 50th, and 100th cycle charged and discharged using 200 mA g^{-1} within the voltage window of 1.5 and 0.01 V and (b) the corresponding cycling stability. (c) The rate capability of *a*-SiNWs/CC electrode at different currents ranging from 0.2 to 5.0 A g^{-1}.(d) Long-term cycling performance of *a*-SiNWs/CC electrode at a current density of 1 A g^{-1} for 350 cycles.

20. The half-cell performance of pure carbon cloth electrode

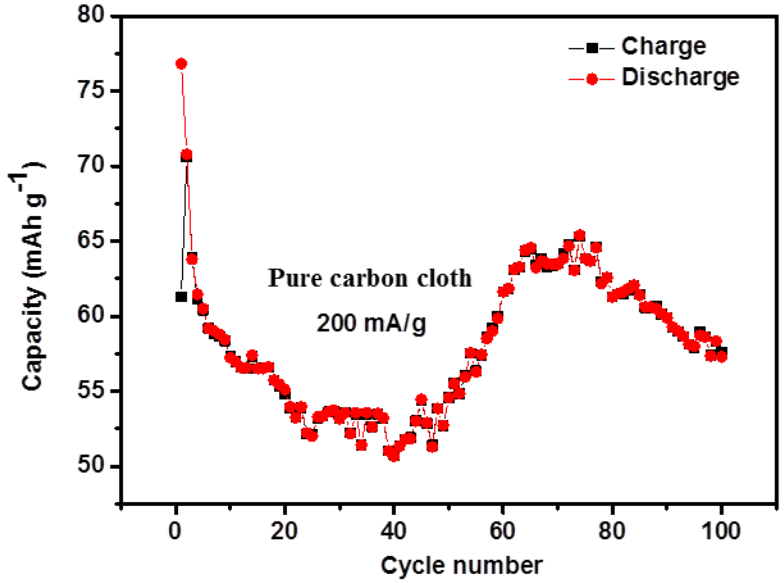

Fig. S18 Cycling performance of pure carbon cloth electrode under a current density of 200 mA g^{-1}.

21. The full cell performance of *a*-SiNWs/CC electrode

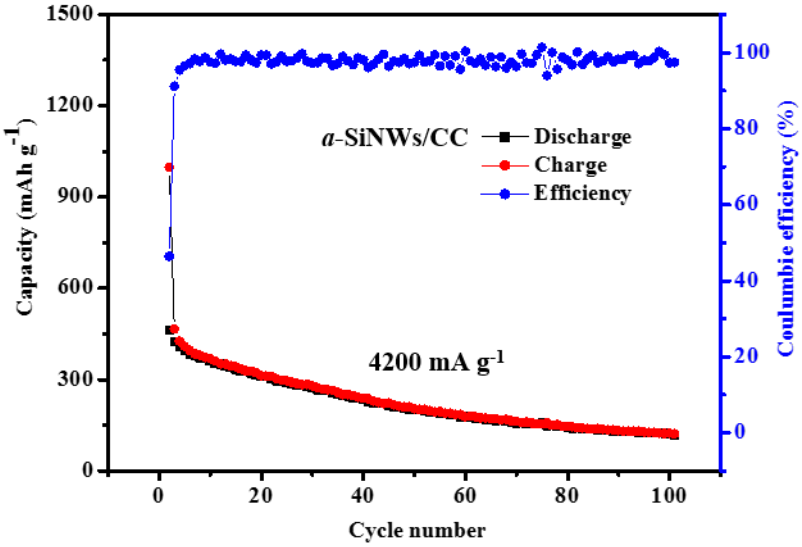

Fig. S19 Cycling performance of *a*-SiNWs/CC electrode with mass loading of 1.42 mg at a current of 4200 mA g^{-1} for 100 cycles.

The electrochemical analysis was carried out at 25℃ with a CR2032 coin-type full-cell using a commercial $LiFePO_4$ (LFP) cathode as the counter electrode in the potential range between 2.5 and 4.2 V. As shown in Fig. S19, the *a*-SiNWs/CC exhibits an initial charge capacity of 998 mAh g^{-1}, corresponding to an initial Coulombic efficiency of 46%, and a capacity of 121 mAh g^{-1} for 100 cycles.

22. The electrochemical performance comparison of silicon anode

Table S6 The electrochemical performance comparison of silicon anode.

Electrode	First cycle capacity	Cycle performance	Full cell
A-SiNWs/carbon cloth (**this work**)	3975 mAh g^{-1} (200 mA g^{-1}), 1872 mAh g^{-1} (1 A g^{-1})	2793 mAh g^{-1} for 100 cycles (200 mA g^{-1}), 1799 mAh g^{-1} for 350 cycles (1 A g^{-1})	998 mAh g^{-1} for first cycle (4200 mA g^{-1}), 121 mAh g^{-1} for 100 cycles (4200 mA g^{-1})
Porous Si microparticles supported by carbon nanotubes[56]	1841.4 mAh g^{-1} (100 mA g^{-1})	796.9 mAh g^{-1} for 100 cycles (500 mA g^{-1}), 600.5 mAh g^{-1} for 300 cycles (1 A g^{-1})	169.4 mAh g^{-1} for first cycle (14.5 mA g^{-1}), 94.3 mAh g^{-1} for 200 cycles (145 mA g^{-1})
A silicon carbon composite material (Si@3DC) in which Si nanoparticles were anchored on a three-dimensional carbon framework through carbon films[57]	2650 mAh g^{-1} (100 mA g^{-1})	305 mAh g^{-1} for 500 cycles (500 mA g^{-1}), 1588 mAh g^{-1} for 1000 cycles (2 A g^{-1})	129 mAh g-1 for 200 cycles (170 mA g^{-1})
One-dimensional tubular silicon-nitrogen doped carbon composite with a core-shell structure[58]	2036.8 mAh g^{-1} (200 mA g^{-1}), 1382.5 mAh g^{-1} (500 mA g^{-1})	583.6 mAh g^{-1} for 200 cycles (500 mA g^{-1})	173.5 mAh g^{-1} for first cycle (200 mA g^{-1}), 79.2 mAh g^{-1} for 100 cycles (200 mA g^{-1})
Silicon doped graphene material[59]	260 mAh g^{-1} (1 A g^{-1})	714 mAh g^{-1} for 400 cycles (1 A g^{-1}), 145 mAh g^{-1} for 400 cycles (5 A g^{-1})	the capacity retention is 86% for 200 cycles (1C)
Si nanotubes[60]	3394 mAh g^{-1} (200 mA g^{-1})	2021 mAh g^{-1} for 100 cycles (200 mA g^{-1}), 1033 mAh g^{-1} for 1000 cycles (1 A g^{-1})	104 mAh g^{-1} for first cycle (1C), 41 mAh g^{-1} for 100 cycles (1C)
Silicon hollow nanocage modified by the carbon[61]	2353 mAh g^{-1} (100 mA g^{-1}), 2360 mAh g^{-1} (500 mA g^{-1})	1506 mAh g^{-1} for 200 cycles (500 mA g^{-1})	Capacity retention of 83% for 200 cycles (45 mA g^{-1})
Porous Si/carbon composite[62]	1319.7 mAh g^{-1} (200 mA g^{-1})	1022 mAh g^{-1} for 100 cycles (200 mA g^{-1})	145 mAh g^{-1} for first cycle (34 mA g^{-1}), 115 mAh g^{-1} for 50 cycles (34 mA g^{-1})

Si/carbon nanotube composites[63]	1769 mAh g^{-1} (100 mA g^{-1})	724 mAh g^{-1} for 300 cycles (500 mA g^{-1})	103 mAh g^{-1} for first cycle (180 mA g^{-1}), 79 mAh g^{-1} for 100 cycles (180 mA g^{-1})
Silicon/graphene/carbon nanocomposite[64]	2213mAh g^{-1} (200 mA g^{-1})	1770 mAh g^{-1} for 200 cycles (200 mA g^{-1})	Capacity retention of 91% for 300 cycles (C/2)
Porous Si[65]	3758.4 mAh g^{-1} (1 A g^{-1})	1383.3 mAh g^{-1} for 500 cycles (1 A g^{-1})	180.1 mAh g^{-1} for first cycle (80 mA g^{-1}), 100.2 mAh g^{-1} for 100 cycles (80 mA g^{-1})
Hollow nitrogen-doped carbon microspheres containing Si nanoparticles[66]	1315 mAh g^{-1} (200 mA g^{-1})	872 mAh g^{-1} for 360 cycles (200 mA g^{-1})	133 mAh g^{-1} for first cycle (340 mA g^{-1}), 60 mAh g^{-1} for 120 cycles (340 mA g^{-1})
Two-dimensional porous amorphous Si nanoflakes and carbon nanotubes composite[67]	2766 mAh g^{-1} (200 mA g^{-1}), 2360 mAh g^{-1} (500 mA g^{-1})	1556 mAh g^{-1} for 100 cycles (200 mA g^{-1}), 844.9 mAh g^{-1} for 200 cycles (1600 mA g^{-1})	139.8 mAh g^{-1} for first cycle (50 mA g^{-1}), 140.5 mAh g^{-1} for 40 cycles (50 mA g^{-1})
Graphene nano-scroll coated silicon nanoparticles[68]	2037.7 mAh g^{-1} (200 mA g^{-1})	1038.2 mAh g-1 for 100 cycles (1 A g^{-1}), 844.9 mAh g-1 for 200 cycles (1600 mA g^{-1})	Capacity retention of 89% for 65 cycles (0.5C)
Carbon-coated mesoporous silicon[69]	1204 mAh g^{-1} (50 mA g^{-1})	564 mAh g-1 for 200 cycles (500 mA g^{-1})	Capacity retention of 88.1% for 200 cycles (0.5C)
Si nanoparticles anchored with CNT to embed into cellulose microscrolls[70]	3254 mAh g^{-1} (200 mA g^{-1})	2056 mAh g-1 for 300 cycles (200 mA g^{-1})	2636 mAh g^{-1} for second cycle (0.3C)

Methods

1. Experimental methods

Amorphous Silicon Nanowires Synthesis

The equipment used in this experiment was consistent with the report[71]. Two kinds of SiC are reversed in our experiment, they are 6H-SiC particles (400 mesh, 97.5%, Aldrich) and α-SiC particles (purchased from Miluo Abrasives General Factory, D_{50}=93 μm). Firstly, made groove (L*W*H=15 mm*15 mm*2 mm) on the surface of commercial graphite block (L*W*H=17 mm*17 mm*10 mm, 99.99%, Beijing Jinglong Special Carbon Technology), and ultrasonically cleaned the customized graphite block with deionized water and absolute ethanol for 20 min, respectively. Furthermore, added 10-80 mg SiC particles to the groove, and put them into the magnetic levitation induction furnace with alumina crucible together. After that, the pure argon gas (99.999%) was introduced into the furnace, and kept the pressure as 2 kPa-1 atm. The process of reversing SiC last 20 s-180 s at a power of 29-32 A by this furnace. Finally, the furnace naturally cooled to room temperature. After the SiC underwent the DMT treatment, it was soaked in HF solution (≥ 40%) at room temperature for 40 min to remove silicon nanowires and expose the surface topography of silicon carbide particles

Cover the purchased carbon cloth (Carbon Energy Technology) over the graphite groove with 6H-SiC particles, react for 20-60 s under 30 A, and then collect silicon nanowires on the carbon cloth.

Half Cell:

(1) Original pure silicon carbide and reverse silicon carbide

The electrochemical performance regarding the reverse SiC has been measured as anode via using CR2032 coin-type half cells, which were assembled in an Ar-filled glove box with lithium metal as the reference electrode. For working electrode preparation, active materials, Super P, and PVDF binder (soluble in NMP) were mixed by grinding them into a slurry with a mass ratio of 7: 2: 1. The resultant slurry was then

uniformly coated on the Cu foil current collector and dried at 80℃ under vacuum for overnight. The active material on the Cu foil as the positive electrode, and the average load was about 0.88-2.2 mg cm^{-2}. The separator is Celgard 2400 membrane, the electrolyte is 1 M $LiPF_6$ in a 1:1 (v/v) mixture of ethylene carbonate (EC) and diethyl carbonate (DEC) with 5 wt% fluorinated ethylene carbonate (FEC). The electrochemical performance was tested with the Neware test system in the voltage range of 0.01-2.0 V.

(2) *a*-SiNWs/CC

The collected *a*-SiNWs on carbon cloth (*a*-SiNWs/CC) was cut into 12 mm diameter electrode sheet and directly applied in lithium-ion half cells. The separator is Celgard 2400 membrane, the electrolyte is 1 M $LiPF_6$ in a 1:1 (v/v) mixture of ethylene carbonate (EC) and diethyl carbonate (DEC) with 5 wt% fluorinated ethylene carbonate (FEC). The electrochemical performance of *a*-SiNWs/CC was tested with the Neware test system in the voltage range of 0.01-1.5 V.

Full Cell. The electrochemical analysis of *a*-SiNWs/CC was carried out with a CR2032 coin-type full cell using a commercial $LiFePO_4$/Al cathode (Canrd, coating surface density is 11.5 mg cm^{-2}, proportion of active substances is 91.5%) as the counter electrode in the potential range between 2.5 and 4.2 V. The electrolyte and diaphragm are the same as the above half cells.

Experimental set-up and conditions:

(1) In the process of applying dynamic magnetic flux to the material, we used a fluxmeter (Tianheng Teslameter, TD8650) and an infrared thermometer (UNI-T50:1 infrared thermometer, UT305S) to characterize the magnetic field and temperature.

(2) Flux changing: The dynamic magnetic flux (DMT) is coming from the flux changing with time. Otherwise, we call it as static field. If we use "I" as the intensity of the magnetic flux, the "I" changing with the time can be expressed as the function: $I=A*ABS(\exp(i(\omega t+\phi_0)))$, where the ω is angular frequency ($\omega=2\pi/T$), and T represents cycling time, and the ϕ_0 is initial phase. This formula conforms to the simple harmonic vibration equation, and the negative part has been rectified into positive ones,

suggesting the magnetic field maintains unchanged. Since the T is 0.02 seconds, the $\omega=2\pi/T=100\ \pi$, therefore the $I_{DMT} = A\exp(i\omega t+\phi_0)=A*ABS(\exp(i*(100\pi+\phi_0)))$. The A and the ϕ_0 depend on the equipment and power, and needs further study.

(3) Frequency and field intensity: The magnetic frequency is around 50 Hz, and the intensity can refer to the equation $I= ABS (A* \exp(i(\omega t+\phi_0)))$.

2. Characterization

The scanning electron microscope (SEM, JSM-7610F，JEOL Ltd., Japan) was used to analyze the morphology of *a*-SiNWs and HF washed the SiC treated under DMT. The morphology and structure of the *a*-SiNWs were investigated by transmission electron microscope (TEM, Titan G2 60-300), with X-ray energy dispersive spectroscopy (EDS) and selected area electron diffraction (SAED). Raman spectra of SiC treated by DMT and as-received SiC was measured with a Raman spectrometer (Thermo Scientific DXR) using 455 nm laser light at room temperature. Raman spectra of *a*-SiNWs was measured with a Raman spectrometer (XploRA PLUS) using 532 nm laser light, and the laser power was 1% of the maximum power. The X-ray diffraction (XRD, D8 ADVANCE A25X, Cu target) was used to characterize the SiC before and after DMT treating. The binding energies of Si, C and O in SiNWS@SiC were measured by X-ray photoelectron spectroscopy (XPS, AXIS Ultra DLD equipped with monochromatic Al Kα source).

References

1. P. R. Bandaru and P. Pichanusakorn, *Semicond. Sci. Tech.*, 2010, **25**, 024003.
2. C. K. Chan, H. Peng, G. Liu, K. McIlwrath, X. F. Zhang, R. A. Huggins and Y. Cui, *Nat. Nanotechnol.*, 2008, **3**, 31-35.
3. J. P. Maranchi, A. F. Hepp and P. N. Kumta, *Electrochem. Solid-State Lett.*, 2003, **6**, A198.
4. J. Yin, M. Wada, K. Yamamoto, Y. Kitano, S. Tanase and T. Sakai, *J. Electrochem. Soc.*, 2006, **153**, A472.
5. S. Misra, L. Yu, M. Foldyna and P. Roca i Cabarrocas, *Sol. Energ. Mat. Sol. C.*, 2013, **118**, 90-95.
6. S. Sharma, K. K. Jain and A. Sharma, *Materials Sciences and Applications*, 2015, **6**, 1145-1155.
7. C. Wu, C. H. Crouch, L. Zhao, J. E. Carey, R. Younkin, J. A. Levinson, E. Mazur, R. M. Farrell, P. Gothoskar and A. Karger, *Appl. Phys. Lett.*, 2001, **78**, 1850-1852.
8. P. Zingway, C. Shu-Tong, L. Chang-Wei and C. Yi-Chan, *IEEE Electr. Device L.*, 2009, **30**, 1305-1307.
9. S. Y. Lim, D. Han, Y. R. Kim and T. D. Chung, *ACS Appl. Mater. Interfaces*, 2017, **9**, 23698-23706.
10. D. Liu, L. Li, Y. Gao, C. Wang, J. Jiang and Y. Xiong, *Angew. Chem. Int. Ed. Engl.*, 2015, **54**, 2980-2985.
11. D. Zhang, Y. Cao, S. K. Karuturi, M. Du, M. Liu, C. Xue, R. Chen, P. Wang, J. Zhang, J. Shi and S. F. Liu, *ACS Appl. Energy Mater.*, 2020, **3**, 4629-4637.
12. K. D. Cantley, A. Subramaniam, R. R. Pratiwadi, H. C. Floresca, J. Wang, H. Stiegler, R. A. Chapman, M. J. Kim and E. M. Vogel, *Appl. Phys. Lett.*, 2010, **97**, 143509.
13. J. Goldberger, A. I. Hochbaum, R. Fan and P. Yang, *Nano Lett.*, 2006, **6**, 973-977.
14. L. Mu, Y. Chang, S. D. Sawtelle, M. Wipf, X. Duan and M. A. Reed, *IEEE Access*, 2015, **3**, 287-302.
15. P. R. Nair and M. A. Alam, *IEEE Trans. Electron Devices*, 2007, **54**, 3400-3408.
16. W. S. Wong, S. Raychaudhuri, R. Lujan, S. Sambandan and R. A. Street, *Nano Lett.*, 2011, **11**, 2214-2218.
17. J. Drowart, G. De Maria and M. G. Inghram, *J. Chem. Phys.*, 1958, **29**, 1015-1021.
18. V. G. Sevast'yanov, P. Y. Nosatenko, V. V. Gorskii, Y. S. Ezhov, D. V. Sevast'yanov, E. P. Simonenko and N. T. Kuznetsov, *Russ. J. Inorg. Chem.*, 2010, **55**, 2073-2088.
19. T. Narushima, T. Goto, Y. Iguchi and T. Hirai, *J. Am. Ceram. Soc.*, 1990, **73**, 3580-3584.
20. S. S. Batsanov, *Inorg. Mater.*, 2001, **37**, 871–885.
21. W. Norimatsu and M. Kusunoki, *Chem. Phys. Lett.*, 2009, **468**, 52-56.

22. Y. Cui, L. J. Lauhon, M. S. Gudiksen, J. Wang and C. M. Lieber, *Appl. Phys. Lett.*, 2001, **78**, 2214-2216.
23. J. Mallet, M. Molinari, F. Martineau, F. Delavoie, P. Fricoteaux and M. Troyon, *Nano Lett.*, 2008, **8**, 3468-3474.
24. V. Schmidt, J. V. Wittemann, S. Senz and U. Gösele, *Adv. Mater.*, 2009, **21**, 2681-2702.
25. R. S. Wagner and W. C. Ellis, *Appl. Phys. Lett.*, 1964, **4**, 89-90.
26. J. Ramanujam, D. Shiri and A. Verma, *Mater. Express*, 2011, **1**, 105-126.
27. L. Schubert, P. Werner, N. D. Zakharov, G. Gerth, F. M. Kolb, L. Long, U. Gösele and T. Y. Tan, *Appl. Phys. Lett.*, 2004, **84**, 4968-4970.
28. G. W. Shim, W. Hong, J.-H. Cha, J. H. Park, K. J. Lee and S.-Y. Choi, *Adv. Mater.*, 2020, **32**, 1907166.
29. N. Fukata, T. Oshima, T. Tsurui, S. Ito and K. Murakami, *Sci. Technol. Adv. Mat.*, 2005, **6**, 628-632.
30. F. Kokai, S. Inoue, H. Hidaka, K. Uchiyama, Y. Takahashi and A. Koshio, *Appl. Phys. A*, 2013, **112**, 1-7.
31. Y. F. Zhang, Y. H. Tang, N. Wang, D. P. Yu, C. S. Lee, I. Bello and S. T. Lee, *Appl. Phys. Lett.*, 1998, **72**, 1835-1837.
32. M. Shao, D. D. D. Ma and S. T. Lee, *Eur. J. Inorg. Chem.*, 2010, **2010**, 4264-4278.
33. F. Wang, A. Dong, J. Sun, R. Tang, H. Yu and W. E. Buhro, *Inorg. Chem.*, 2006, **45**, 7511-7521.
34. W.-S. Shi, H.-Y. Peng, Y.-F. Zheng, N. Wang and N.-G. Shang, *Adv. Mater.*, 2000, **12**, 1343-1345.
35. N. Wang, Y. H. Tang, Y. F. Zhang, C. S. Lee and S. T. Lee, *Phys. Rev. B*, 1998, **58**, R16024.
36. X. Chen, Y. Xing, J. Xu, J. Xiang and D. Yu, *Chem. Phys. Lett.*, 2003, **374**, 626-630.
37. Y. Y. Wong, M. Yahaya, M. Salleh and Y. Majlis, *Sci. Technol. Adv. Mat.*, 2005, **6**, 330-334.
38. D. P. Yu, Y. J. Xing, Q. L. Hang, H. F. Yan, J. Xu, Z. H. Xi and S. Q. Feng, *Physica E* 2001, **9**, 305-309.
39. S. Pinilla, R. Barrio, N. González, R. Pérez Casero, F. Márquez, J. M. Sanz and C. Morant, *J. Phys. Chem. C*, 2018, **122**, 22667-22674.
40. N. Dhindsa, J. Walia, M. Pathirane, I. Khodadad, W. S. Wong and S. S. Saini, *Nanotechnology*, 2016, **27**, 145703.
41. C.-M. Hsu, S. T. Connor, M. X. Tang and Y. Cui, *Appl. Phys. Lett.*, 2008, **93**, 133109.
42. J. Zhu, Z. Yu, G. F. Burkhard, C.-M. Hsu, S. T. Connor, Y. Xu, Q. Wang, M. McGehee, S. Fan and Y. Cui, *Nano Lett.*, 2009, **9**, 279-282.
43. S. Thomas, J. Mallet, F. Martineau, H. Rinnert and M. Molinari, *ACS Photonics*, 2018, **5**, 2652-2660.
44. M. N. M. Nor, U. Hashim, N. H. A. Halim and N. H. N. Hamat, *AIP Conference Proceedings. American Institute of Physics*, 2010, **1217**, 272-278.

45. R.-Q. Zhang, Y. Lifshitz and S.-T. Lee, *Adv. Mater.*, 2003, **15**, 635-640.
46. Ü. Sökmen, A. Stranz, S. Fündling, H. H. Wehmann, V. Bandalo, A. Bora, M. Tornow, A. Waag and E. Peiner, *J. Micromech. Microeng.*, 2009, **19**, 105005.
47. Y. Cao, Y. Zhou, F. Liu, Y. Zhou, Y. Zhang, Y. Liu and Y. Guo, *Ecs J. Solid State Sc.*, 2015, **4**, P331-P336.
48. J. T. Harris, J. L. Hueso and B. A. Korgel, *Chem. Mater.*, 2010, **22**, 6378-6383.
49. Q. Huang, G. Wang, L. Guo, Y. Jia, J. Lin, K. Li, W. Wang and X. Chen, *Small*, 2011, **7**, 450-454.
50. M. Kusunoki, T. Suzuki, T. Hirayama, N. Shibata and K. Kaneko, *Appl. Phys. Lett.*, 2000, **77**, 531-533.
51. S. Wang, X. Yuan, X. Bi, X. Wang and Q. Huang, *Phys. Chem. Chem. Phys.*, 2015, **17**, 23711-23715.
52. Q. Liu, R. Qi, S. Song, Z. Yan and Q. Huang, *ChemComm*, 2018, **54**, 12694-12697.
53. Y. Jia, L. Guo, W. Lu, Y. Guo, J. Lin, K. Zhu, L. Chen, Q. Huang, J. Huang, Z. Li and X. Chen, *Sci China-Phys. Mech. Astron.*, 2014, **56**, 2386-2394.
54. K. Zhu, L. Guo, J. Lin, W. Hao, J. Shang, Y. Jia, L. Chen, S. Jin, W. Wang and X. Chen, *Appl. Phy. Lett.*, 2012, **100**, 023113.
55. K. V. Emtsev, A. Bostwick, K. Horn, J. Jobst, G. L. Kellogg, L. Ley, J. L. McChesney, T. Ohta, S. A. Reshanov, J. Röhrl, E. Rotenberg, A. K. Schmid, D. Waldmann, H. B. Weber and T. Seyller, *Nat. Mater.* , 2009, **8**, 203-207.
56. Q. Zhang, B. Xi, W. Chen, J. Feng, Y. Qian and S. Xiong, *Nano Res.*, 2022, **15**, 6184-6191.
57. F. Wu, Z. He, M. Wang, Y. Huang and F. Wang, *Nano Res.*, 2022, **15**, 6168-6175.
58. J. Zhao, W. Wei, N. Xu, X. Wang, L. Chang, L. Wang, L. Fang, Z. Le and P. Nie, *Chemphyschem : a European journal of chemical physics and physical chemistry*, 2022, **23**, e202100832.
59. H. Liu, W. Yang, S. Che, Y. Li, C. Xu, X. Wang, G. Ma, G. Huang and Y. Li, *Carbon*, 2022, **196**, 633-638.
60. F. Wang, P. Li, W. Li and D. Wang, *ACS Nano*, 2022, **16**, 7689-7700.
61. H. Xue, Y. Wu, Z. Wang, Y. Shen, Q. Sun, G. Liu, D. Yin, L. Wang, Q. Li and J. Ming, *ACS Appl. Mater. Interfaces*, 2021, **13**, 40471-40480.
62. Z. Hou, H. Liu, P. Chen and J. G. Wang, *Part Part Syst Charact*, 2021, **38**, 2100107.
63. S. Mei, Y. Liu, J. Fu, S. Guo, J. Deng, X. Peng, X. Zhang, B. Gao, K. Huo and P. K. Chu, *Appl. Surf. Sci.*, 2021, **563**, 150280.
64. S. Abouali, M. A. Garakani, L. Silvestri, E. Venezia, L. Marasco and R. Brescia, *2D Mater.*, 2021, **8**, 035014.
65. C. Zhang, Q. Ma, M. Cai, Z. Zhao, H. Xie, Z. Ning, D. Wang and H. Yin, *Waste Manage.*, 2021, **135**, 182-189.
66. L. Yin, M. Park, I. Jeon, J. H. Hwang, J. P. Kim, H. W. Lee, M. Park, S. Y. Jeong and C.-R. Cho, *Electrochim. Acta*, 2021, **368**, 137630.
67. Z. Wang, Y. Li, S. Huang, L. Liu, Y. Wang, J. Jin, D. Kong, L. Zhang and O. G. Schmidt, *J. Mater. Chem. A*, 2020, **8**, 4836-4843.

68. M. Shi, P. Nie, Z. Fan, R. Fu, S. Fang, H. Dou and X. Zhang, *Front. Energy Res.*, 2020, **8**, 1-9.
69. H. Park, N. Yoon, D. Kang, C. Young and J. K. Lee, *Electrochim. Acta*, 2020, **357**.
70. H. Wang, J. Fu, C. Wang, J. Wang, A. Yang, C. Li, Q. Sun, Y. Cui and H. Li, *Energy Environ. Sci.*, 2020, **13**, 848-858.
71. C. Wu, R. Qi, X. Zhang, Q. Liu and Q. Huang, *ChemComm*, 2019, **55**, 7522-7525.